RESEARCH PAPER

Novel high performance mixed matrix nanocomposites membranes: its structural, morphology, thermal stabilities, mechanical properties, gas permeation and gas selectivity studies

Hashem Ahmadizadegan* , Sheida Esmaielzadeh

[1] *Department of Chemistry, Darab branch, Islamic Azad University, Darab, Islamic Republic of Iran*

ARTICLE INFO

Article History:
Received 22 October 2019
Accepted 15 January 2020
Published 15 February 2020

Keywords:
Polyimide
Nanocomposites
Modified LDHs
Coprecipitation

ABSTRACT

Modified LDHs particles, including LDH-amino benzoate (M-LDHs) nanoparticles with the intercalated amino benzoate in the interlayer galleries are well exfoliated and show excellent compatibility in the polyimide (PI) matrix. Using FT-IR spectroscopy, X-ray diffraction (XRD), FE-SEM, and electron microscopy (TEM), we confirmed that M-LDHs/PI nanocomposites were successfully synthesized. PI hybrid films with different contents of M-LDHs nanoparticles (0, 3, 5 and 7 wt%) were compared in terms of their morphologies, thermal properties, and gas permeation and selectivity properties. We used TEM to evaluate the degree of intercalation and the amount of aggregation of the M-LDHs nanoparticles. The M-LDHs nanoparticles, for the most part, were well dispersed in the polymer matrix. Moreover, the addition of only a small amount of LDHs particles was enough to improve the thermal stabilities and mechanical properties of PI hybrid films. The thermo-optical properties were measured by differential scanning calorimetry (DSC), thermogravimetric analysis (TGA), and ultraviolet-visible (UV–Vis) spectrometry. As anticipated, though the gas permeability of pure gases, such as He, N_2, CH_4 and CO_2 exhibited a decrease, it was not monotonous. A marked decrease in permeability of gases such as CO_2 and CH_4, in comparison to relatively lower decrease in permeability of He, was observed, especially at higher LDH loading. An increase in selectivity: α(He/CO_2) and α(He/CH_4), especially at higher LDH loading indicated the capability of nanocomposites to tune the selectivity favorably.

How to cite this article
Ahmadizadegan H., Esmaielzadeh Sh.. Novel high performance mixed matrix nanocomposites membranes: its structural, morphology, thermal stabilities, mechanical properties, gas permeation and gas selectivity studies. Nanochem Res, 2020; 5(1):77-93. DOI: 10.22036/ncr.2020.01.008

INTRODUCTION

Polymer/clay nanocomposites have attracted great academic and industrial interests in recent years because they exhibit unique microstructure with enhanced mechanical, thermal and barrier properties compared with conventional microcomposite at identical filler concentrations [1–4]. It is noteworthy that chemical modification of nanoparticles such as clay prior to their incorporation into polymer nanocomposites provides a convenient route to improve dispersion and to modify interfacial properties that may in turn improve the properties of the nanocomposites. Polyimide (PI) is widely used in the field of microelectronics and photonics application, because of their outstanding electrical properties, heat resistance, and chemical stability [5-8].

Various combinations of polyimide with inorganic fillers including silica, layered silicate, graphene, alumina have been reported, showing that outstanding mechanical and physical properties can be achieved when proper contents of fine fillers are incorporated. Especially, the layered

* Corresponding Author Email: *h.ahmadizadegan.2005@gmail.com*

silicate clay particles, such as montmorillonite or mica, when the layers of clay are organic, exfoliated or intercalated [9], can be well dispersed and much more effective to reinforce the performance of polymer. The composites prepared from polyimide and layered clay by solution dispersion technique or in situ polymerization have been found to display novel properties [10]. It was noticed that the introduction of well dispersed clay layers such as montmorillonite (MMT) into a polyimide matrix has been proved to be extremely effective in the improvement of mechanical, thermal and barrier properties of the polyimide matrix.

Clays are used as additives because they are composed of layered silicates that can intercalate organic molecules [11, 12]. The morphology of clay particles has been described in several papers [13]. There are many types of clays, including kaolinite, montmorillonite, hectorite, saponite, and synthetic mica. Among them a new promising class of inorganic layered materials; e.g., layered double hydroxides (LDHs), have been attracting much attention because of their wide applications in catalysts, catalyst precursors, anion exchangers, fire retardants, hydrogenation reaction, acid absorbents, bioactive nanocomposites, electroactive and photoactive materials, etc [14-16] . Layered double hydroxides (LDHs), also known as anionic or hydrotalcite-like clays, are a class of lamellar compounds having overall no charge (neutral) due to the existence of positively charged brucite-like hydroxide layers with typical thickness 0.48 nm and hydrated exchangeable anions located in the interlayer gallery [17]. The positive charge of the brucite-like layers arises from the partially isomorphous substitution of trivalent cations for divalent metal ones. Due to their highly tunable properties and unique anion exchange properties, LDHs are considered as a new emerging and the most favorable class of layered crystals for fabricating of multifunctional polymer/ layered inorganic nanocomposites [18].

As well as the well dispersion of the clay nanolayers in the polymer matrix, the interfacial interaction between the inorganic and organic phases is important for the improvement of the performance in the nanocomposites. Therefore, as the scale-length of the inorganic fillers approaches the nanometer range, the extent of phase separation reduces and improves the performance of the nanocomposites. In addition, the introduction of chemical bondings between inorganic and organic phases can effectively enhance the interfacial interaction, being a key issue in preparing the compatible nanocomposites exhibiting excellent performance [19-24].

Although polymer/clay nanocomposites are known to exhibit gas barrier properties better than those of conventional composite systems, the dependence of these properties on factors such as the orientations of the matrix sheets and the extent of clay aggregation and dispersion (intercalation, exfoliation, or intermediate structures) are not well understood [14, 25]. Bharadwaj [26] constructed a model for the barrier properties in polymer-layered silicate nanocomposites based completely upon the tortuosity arguments described by Nielsen. [27]. The correlations among sheet length, concentration, relative orientation, and aggregation state are expected to provide guidance in the design of better barrier materials with the nanocomposite approach [28].

To date, experimental data on clay–polymer hybrid membrane for gas separation purpose are still diminutive in contrast to other filler–polymer combinations. In fact, the compatibility of most hydrophobic thermoplastic polymers with commercially modified clay minerals has been confirmed in the literature [29, 30]. Moreover, the clay modification, commonly achieved by cationic-exchange reaction with alkylammonium surfactants, leads to the expansion of interlayer space of the clay. The pre-expanded state of the clay layers will facilitate the intercalation of polymer macromolecules into the interlayer galleries thus rendering greater extent of interaction and dispersion of silicate layers in polymer matrix [31-33]. Modified LDHs particles (M-LDHs) are an example of available modified clay which will be used in this study. As for the continuous phase, polyimide (PI) is a fine choice of membrane material for gas separation due to practical combination between its permeability and selectivity in addition to its good mechanical and thermal properties as well as easy processability.

We prepared new nanocomposite films comprised of modified LDHs particles, including LDH-amino benzoate (M-LDHs) and PI obtained from diamine monomer (diamine1B) and pyromelliticdianhydride (PMDA) monomers. The effect of the M-LDHs particles in a PI hybrid system was examined for different amounts of M-LDHs (1, 3, 5 or 7 wt%). The thermal properties, morphologies, gas permeation, and mechanical properties of the resultant PI hybrid films with various amounts of M-LDHs are reported herein.

EXPERIMENTS

Materials

2-(2-hydroxy-5-methylphenylsulfinyl)-4-methylphenol and 1-chloro-4-nitrobenzene and potassium carbonate were purchased from TCI (Tokyo, Japan) and Aldrich Chemical Co. (Seoul, Korea). N,N-dimethylacetamide (DMAc) was purified and dried over molecular sieves before use. All other reagents were used without further purification. PMDA was recrystallized from acetic anhydride and then dried in a vacuum oven at 120°C overnight. $Mg(NO_3)_2$ $6H_2O$ (Riedel-deHaen), $Al(NO_3)_3$ $9H_2O$ (Riedel-deHaen), sodium hydroxide (Riedel-deHaen), sodium carbonate (Aldrich Chemical Co) and amino benzoic acid (Riedel-deHaen) were used to synthesize the amino benzoate intercalated layered double hydroxides (LDHs).

Equipment

Fourier transform infrared (FTIR) spectra were recorded using a Nicolet 360 IR spectrometer. Wide-angle X-ray diffraction (XRD) measurements were performed at room temperature using a Rigaku (D/Max-IIIB) X-ray diffractometer with Ni-filtered CuKα radiation. The scan rate was 20/min over the range 2θ=2°-23°. Transmission electron microscopy (TEM) photographs of ultrathin sections of the PI hybrid films were obtained with a Leo 912 OMEGA transmission electron microscope using an acceleration voltage of 120 kV. Differential scanning calorimetry (DSC) and thermogravimetric analysis (TGA) were performed on a DuPont 910 instrument with a heating rate of 20 °C/min under N_2 flow. The measurements of the coefficients of thermal expansion (CTE) of the samples were performed with a macroexpansion probe (TMA-2940), which was used to apply a 0.1 N expansion force to the films at a heating rate of 5 °C/min in the temperature range 40-170 °C. The permeability of the films was measured according to the ASTM E96 standards using a Mocon DL 100. Ultraviolet visible (UV-Vis) spectra of the polymer films were recorded using a Shimadzu UV-3600 instrument.

Synthesis of diamine monomer (1B)

In a 50 mL three-neckround-bottom flask, 2-(2-hydroxy-5-methylphenylsulfinyl)-4-methylphenol (1.81 g, 6.8mmol), 1-chloro-4-nitrobenzene (2.03 g, 13.6mmol), potassium carbonate (1.87 g, 13.6mmol), and 15 mL of DMAc were placed. The mixture was heated with stirring at 125 °C for 5 h under nitrogen. The reaction mixture was cooled and then poured into 250 mL of methanol. The creamy precipitate was collected by filtration and dried under vacuum. The product was purified by recrystallization from glacial acetic acid to afford monomer (1A) in 89% yield; mp 213-215 °C. Second step, hydrazine monohydrate (3 mL) was added dropwise to a mixture of dinitro (1A) (1.80 g, 3.6mmol), ethanol (25 mL), and a catalytic amount of 10% palladium on activated carbon (Pd/C, 0.04 g) at the boiling temperature. The mixture became homogeneous after 2 h, and the reaction was refluxed for 18h. The mixture was then filtered to remove Pd/C. After cooling, the precipitated yellow crystals were isolated by recrystallization. It was purified by recrystallized from methanol and then sublimed before use in polymerization (Scheme 1). The yield was 78%; mp 170-173 °C [34].

The molecular structure of diamine (1B) was confirmed with elemental, IR, ^{1}H-NMR and ^{13}C-NMR analyses. The familiar double absorption peaks of amine groups N–H are obvious around 3445–3397 cm^{-1}.The ^{1}H-NMR data confirm the proposed structure for diamine (1B). Signal peak resonated at 4.597 ppm is related to the amino protons -NH_2. The ^{13}C-NMR data indicated the presented chemical structure of diamine (1B) clearly. All the spectroscopic data obtained were in good agreement with the expected structure of diamine (1B) [34].

FTIR (KBr, cm^{-1}): 3,445 (s), 3,397 (s), 3,113 (w), 3,080(w), 1,565 (m), 1,545 (m) 1,439 (w), 1,336(w), 1,157 (w), 833(m), 775(w).

^{1}H-NMR (500 MHz, DMSO-d_6, ppm): 2.367 (s, 6H, CH), 4.597 (s,4H, NH), 6.654-6.661 (d, 4H, Ar-H, *J*= 3.5), 6.869-6.878 (d, 2H, Ar-H, *J*= 4.5 Hz), 7.349-7.357 (d, 4H, Ar-H),7.629 (s, 2H, Ar-H).

^{13}C-NMR (125 MHz, DMSO-d_6), δ (ppm): 39.55 (CH_3), 109.11 (Ar), 110.09 (Ar), 115.61 (Ar), 118.66 (Ar), 122.20 (Ar), 124.59 (Ar), 132.47(Ar),138.75(Ar), 146.65(Ar), 154.75(Ar).

Elemental analysis calculated for $C_{26}H_{24}N_2O_3S$ (444.15g mol^{-1}): C, 70.27%; N, 6.29%; S, 7.19%;H, 5.45 %.

Preparation of the modified LDHs-amino benzoate (M-LDHs)

The LDHs-amino benzoate was prepared by the co-precipitation method. 0.8 g (0.02 mol) of NaOH was dissolved in 200 ml of deionic water, and then, 3.74 g (0.02 moel) of 4-amino benzoic acid was

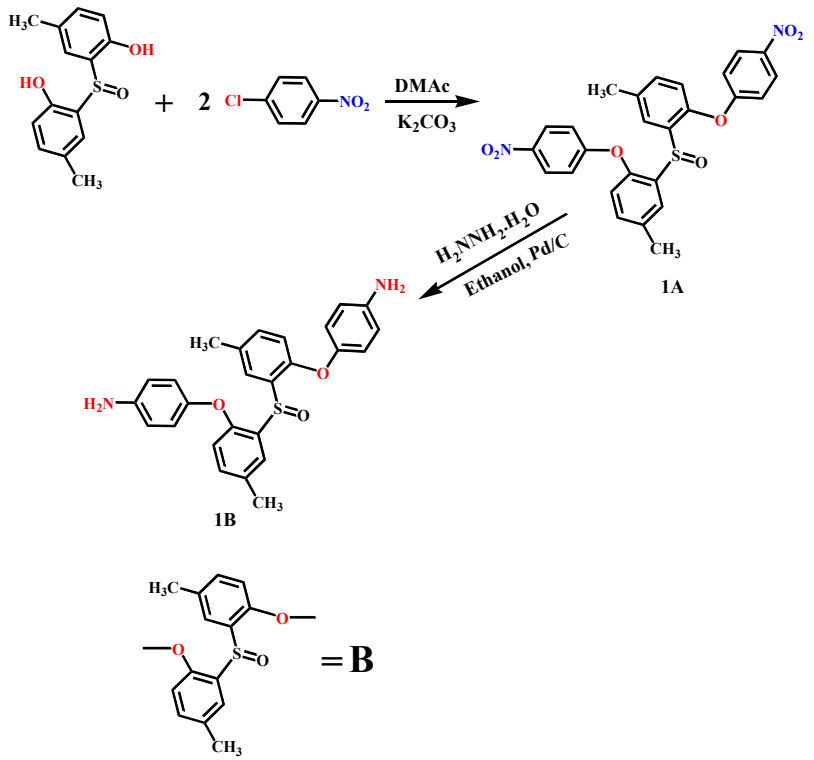

Scheme 1. Synthesis of a novel monomer diamine (1B).

added to the sodium hydroxide solution. 5.12 g (0.02 mol) of magnesium nitrate and 3.75 g (0.01 mol) of aluminum nitrate were dissolved in 50 ml of deionic water. The nitrate solution was then added dropwise to the vigorously stirred amino benzoate/NaOH solution at room temperature and the pH of the solution was maintained at 10 by the addition of 1 M NaOH solution. After the addition of the nitrate solution, the mixture was reacted at 75 °C for 16 h. The slurry was then filtered until all the supernatant liquid were removed. The sample was washed four times by doubly deionic water and dried at 70 °C. In order to minimize contamination with atmospheric CO_2, the preparation of the LDH-AB was performed under a nitrogen purge [35].

Preparation of the PI Hybrid Films

The PI films were synthesized using a two-step method. First, diamine 1B (1.55 g, 3.5 mmol) was added into a flask and dissolved in the DMAc with stirring. After 0.5 h, diamine 1B was dissolved completely, and 0.75 g PMDA (3.50 mmol) was added into the above solution. The resulting solution was stirred vigorously at 0 °C for 1 h and then at room temperature for 10 h, yielding a 20 wt% DMAc solution of PAA. The synthetic procedures for polymer hybrid preparation were the same for all clay contents used; the preparation of 10 wt% M-LDHs is detailed here as a representative example. M-LDHs (1.0 g) and DMAc (30 mL) were placed in a 100 mL three-necked flask, and the mixture was stirred at 25 °C for 2 h. The resulting mixture was ultrasonicated for 7 h to obtain a homogeneously dispersed clay solution. In the chemical imidization procedure for the PAA solution, isoquinoline (3-4 drops) was added to the PAA solution, and the mixture was stirred at 25 °C for 2 h under a steady stream of N_2 gas. The composite solution was cast onto glass plates, and then the solution was stabilized at 50 °C for 1 h under a steady stream of N_2 gas. After that, sequential heat treatments were performed at 70 °C for 1 h and 80 °C for 2 h. The film was further imidized on the glass plate by sequential heating at 110, 140, 170, 200, and 250 °C for 30 min at each temperature. The film was cooled to room temperature and stripped from the glass in hot water. The chemical structures relevant to the synthetic route are also shown in Scheme 2 and Scheme 3 [20].

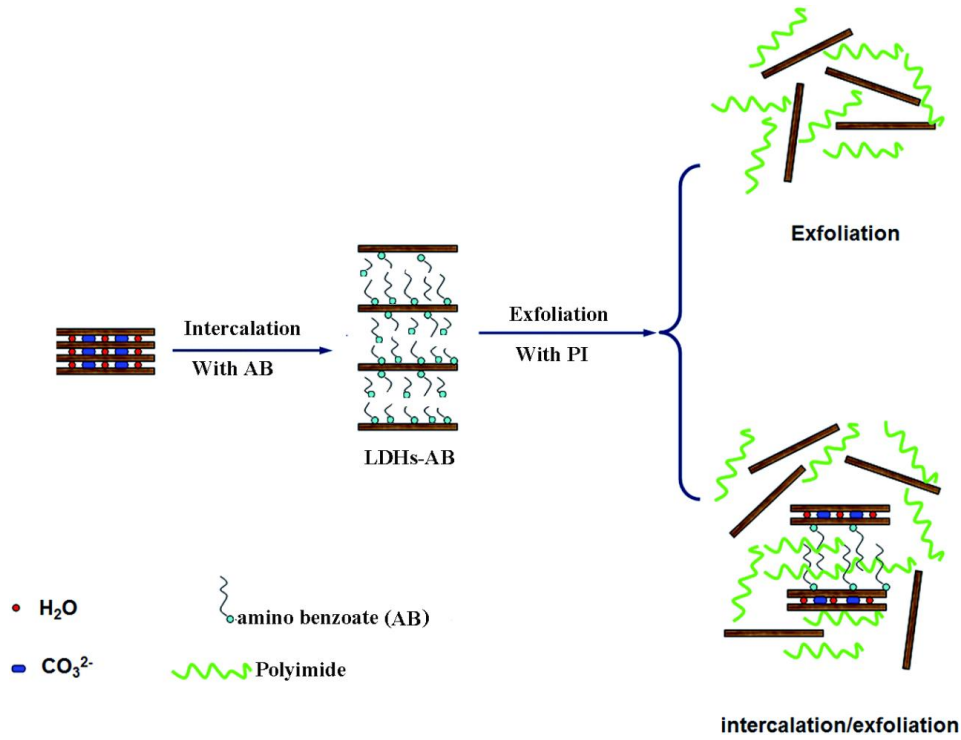

Scheme 2. Schematic representation of the M-LDHs intercalation and the exfoliated M-LDHs/PI nanocomposites

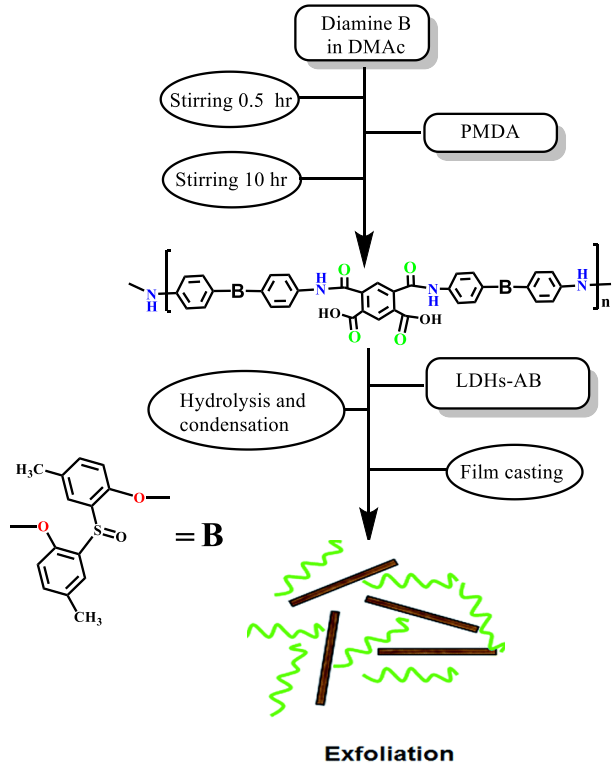

Scheme 3. Synthetic routes to M-LDHs/PI nanocomposites using a two-step method.

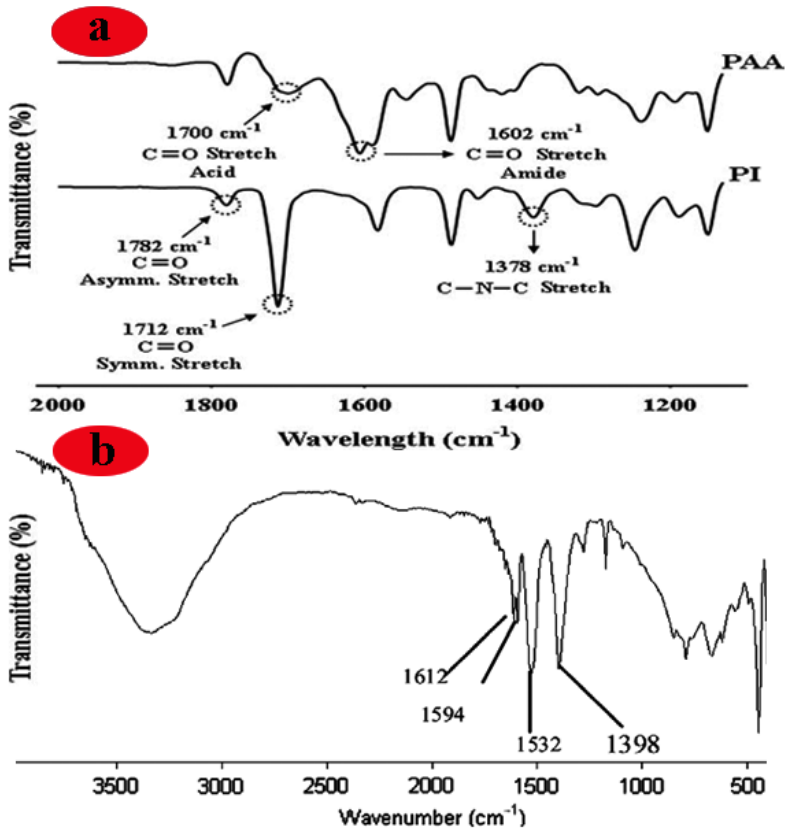

Fig. 1. FT-IR spectrum of PAA and PI (a) and M-LDHs (b).

RESULTS AND DISCUSSION

FTIR spectra of PAA and PI and M-LDHs

The formation of PAA and the completion of imide formation from amic acid were confirmed by examining the FT-IR spectra; the spectra of PAA and the PIs are shown in Fig. 1a. It was observed that PAA exhibited a broad absorption band around 2800-3400 cm^{-1} because of the acid (O-H) group of PAA. The C=O stretching peaks at 1700 and 1602 cm^{-1} are due to the acid and amide groups of PAA [21], respectively, and shift to higher frequencies in the imides, specifically to approximately 1782 cm^{-1} (C=O, in phase) and 1712 cm^{-1} (C=O, out of phase), respectively. In addition, the presence of a feature at 1378 cm^{-1} corresponding to C-N-C stretching confirms the formation of the imides [15, 21, 23].

Fig. 1b presents the FT-IR spectrum of the M-LDHs. Strong absorption peaks of asymmetric and symmetric R–COO^- at 1532 and 1398 cm^{-1}, respectively, are observed. The characteristic peaks of the N–H bend and aromatic C=C stretching are at 1612 and 1594 cm^{-1}, respectively [12, 15, 21, 23, 29]. These peaks demonstrate that amino benzoate was intercalated into the LDHs. A broad absorption peak between 3600 and 3000 cm^{-1} is assigned to O–H group stretches of both the hydroxide layers and the interlayer water [29, 30].

XRD patterns of the M-LDHs and M-LDHs/PI nanocomposites

Fig. 2a presents the X-ray patterns of the M-LDHs nanocomposite. The observed data show an increase to 15Å (2θ = 5.5°) for M-LDHs. An expanded structure is obtained and two peaks are present at 2θ = 5.5° and 2θ = 11.4°, indicating that amino benzoate and carbonate are both present in the interlayer galleries of M-LDHs. From the results, not only the amino benzoate but also the carbonate are intercalated into M-LDHs, and the carbonate content is far less than the amino benzoate content. This finding may justify the involvement of less CO_2 molecules in the preparation of the M-LDHs powder. The processing conditions used in the preparation of the M-LDHs/PI nanocomposites

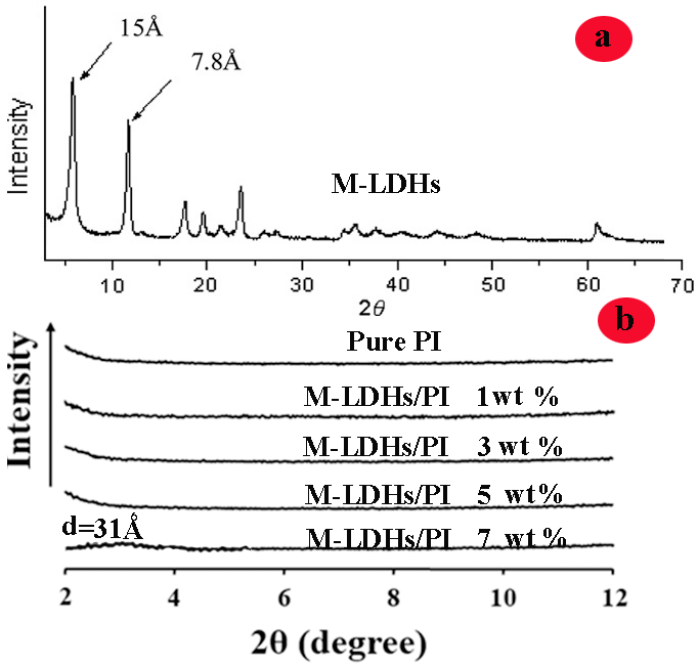

Fig 2. XRD patterns of M-LDHs (a) and M-LDHs/PI nanohybrid films with various M-LDHs contents (b).

significantly affect the extent of exfoliation of the M-LDHs nanolayers in the polymer matrix.

Fig. 2b shows the XRD patterns of the M-LDHs/PI nanocomposites with various M-LDHs contents. For the M-LDHs/PI nanocomposites, no diffraction peak is observed with M-LDHs content from 1 to 5 wt%, while a diffraction peak arises at 3° with the content of 7 wt%. The result is due to the sufficiently exfoliation of the M-LDHs nanolayers in the polymer matrix to form exfoliated nanocomposites M-LDHs with the content from 1 to 5 wt%. In nanohybrids, we found that clay was very uniformly distributed in the PI matrix regardless of the clay concentration. This denotes that the clay layers in the hybrid material are homogeneously dispersed in the PI matrix. As the content of the M-LDHs reaches 7 wt%, an obvious diffraction peak appears at 3°, corresponding to some parts of the clay layer which were collapsed in the PI matrix. It was considered that thermal decomposition of the organic part in M-LDHs resulted in reducing the d-spacing of clay layers. [36] Yano et al. [37] also reported that weakly bound organic molecules may detach from the clay surface. This detachment, caused by the heat treatment during the cyclization process of PAA to PI, leads to a reduction in the interlayer spacing relative to that of M-LDHs.

Morphology of M-LDHs/PI nanocomposites

Although XRD is by far the simplest method available to measure the d-spacing of the hybrids, FE-SEM and TEM were also used to visually evaluate the degree of intercalation and the amount of aggregation of clay clusters. TEM analysis tends to support the findings from XRD but also shows that the clay is well dispersed on the nanoscale in all systems. The efficiency of the clay in modifying the properties of the matrix polymer is primarily determined by the degree of its dispersion in the polymer matrix.

The morphology of the aggregated clay can be characterized with FE-SEM. Because of the difference in scattering density between the M-LDHs and PI, large M-LDHs aggregates can be easily imaged in FE-SEM**.** Figs. 3(b)–(e) show clay phases within the hybrid films with organoclay contents of 1 to 7.0 wt%. The PI hybrid films containing 1 wt% M-LDHs are characterized by clay domains (with sizes of 200–300 nm) dispersed in a continuous PI phase (Fig. 3b). In contrast, the micrograph of the 5.0 wt% M-LDHs/PI hybrid film (Fig. 3d) shows voids and some deformed regions that can be attributed to the coarseness of the fractured surface. This coarseness is aggravated upon increasing the clay content up to 5 wt% (Figs

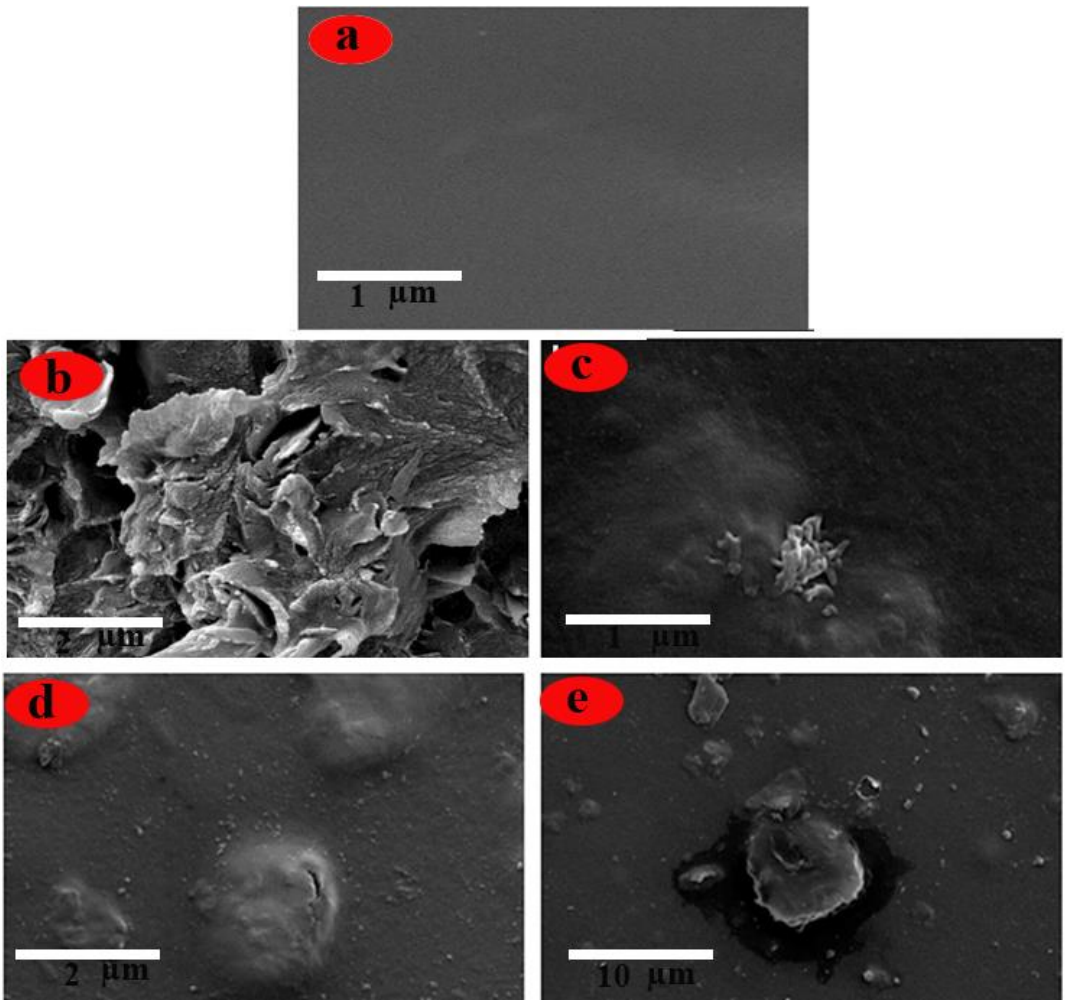

Fig. 3. FE-SEM pictures of pure PI (a) and nanocomposites with various clay loadings: (b) 1%, (b) 3 %, (c) 5 %, and (d) 7%.

3d and e). Comparison of the micrographs reveals that the fractured surfaces of the hybrid films with higher M-LDHs contents are more deformed than those of the films with lower M-LDHs contents, likely due to the agglomeration of M-LDHs particles. This hypothesis is supported by the observation of agglomerated M-LDHs particles in the PI hybrid films with clay contents of 5–7 wt%.

More direct evidence of the formation of a true nanocomposite is provided by TEM of an ultramicrotomed section. Fig. 4(a–d) shows three photographs of PI hybrids containing different 1, 3, 5 and 7 wt % organoclays. The dark lines in the photograph are the intersections of a clay sheet 1 nm thick, and the spaces between the dark lines are interlayer spaces. TEM photography proves that most clay layers have been dispersed homogeneously into the matrix polymer, although some clusters or agglomerated particles are also detected. A similar arrangement of the layers in Fig. 4(c and d) can be observed, with the presence of one or several clay layers in the PI matrix, indicating the formation of nanocomposites. Unlike hybrids containing M-LDHs (Fig. 5(a,b)], the clay layers of Fig. 5(c and d) are more exfoliated and dispersed randomly into the matrix polymer. This will be cross-checked by ultimate strength and initial modulus in the tensile property section.

Mechanical properties of pure PI and M-LDHs/PI nanocomposites

Dynamic mechanical analysis (DMA) for the M-LDHs/PI nanocomposites was carried out to understand the effect of the M-LDHs particles

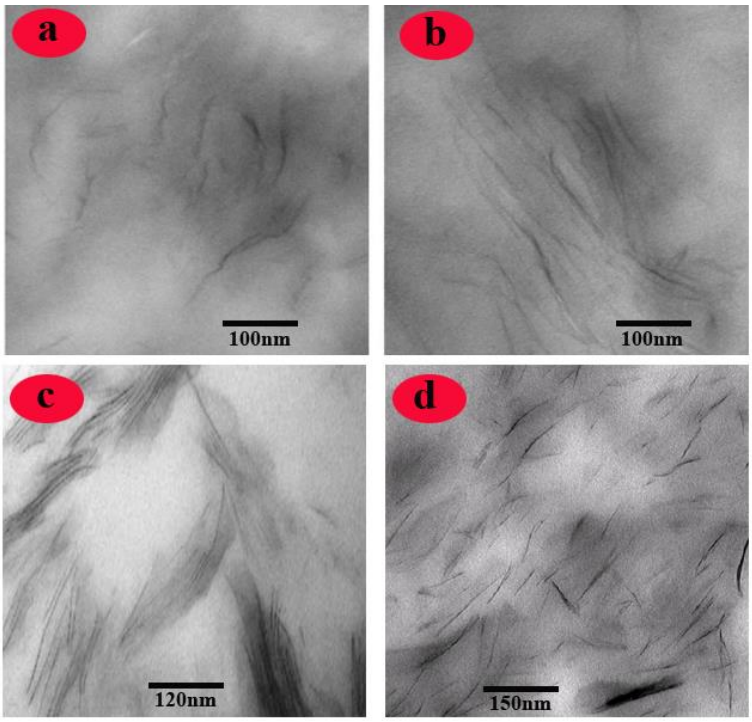

Fig. 4. TEM photographs of PI hybrids containing different 1 wt % (a), 3 wt % (b), 5 wt % (c) and 7 wt % (d) M-LDHs organoclays

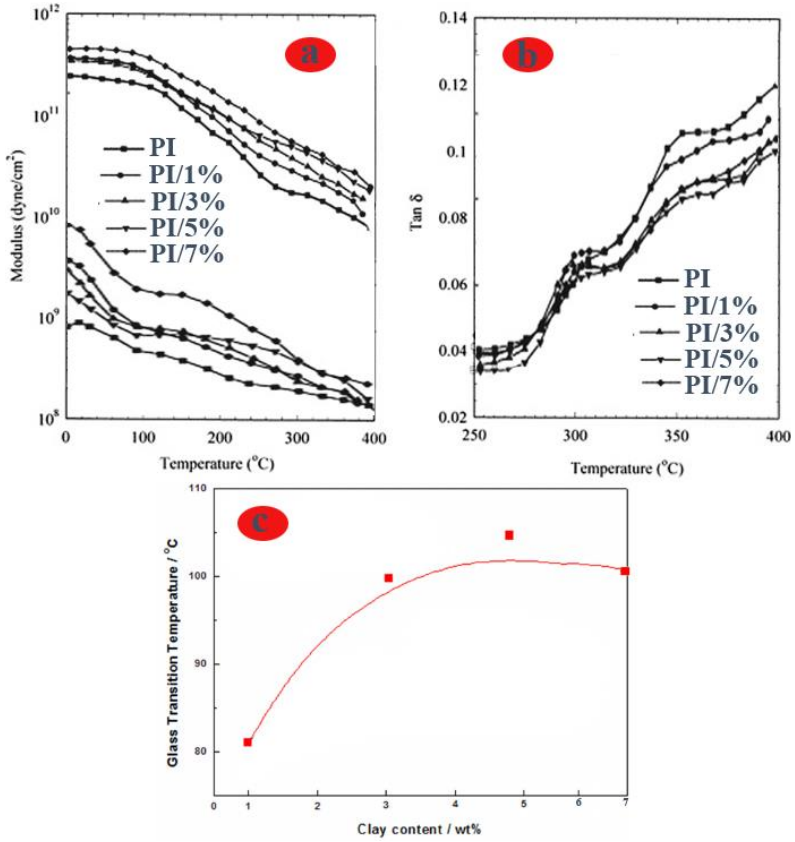

Fig. 5. (a) Dynamic mechanical properties of M-LDHs/PI nanocomposites films with various M-LDHs nanoparticles contents. (b) Tan δ of M-LDHs/PI nanocomposites films with various contents of the M-LDHs nanoparticles. (c) Effect of the M-LDHs nanoparticles content on the T_g value from the maxima of E″ of the M-LDHs/PI nanocomposites.

Table 1. Mechanical properties for the M-LDHs/PI nanocomposite film

Material	E (GPa)[a]	σ (MPa)	Elongation (%)
Pure PI	7.85	245	28.68
M-LDHs/PI 1%	9.86	275	15.05
M-LDHs/PI 3%	11.68	282	11.36
M-LDHs/PI 5%	13.86	188	7.21
M-LDHs/PI 7%	11.81	161	6.89

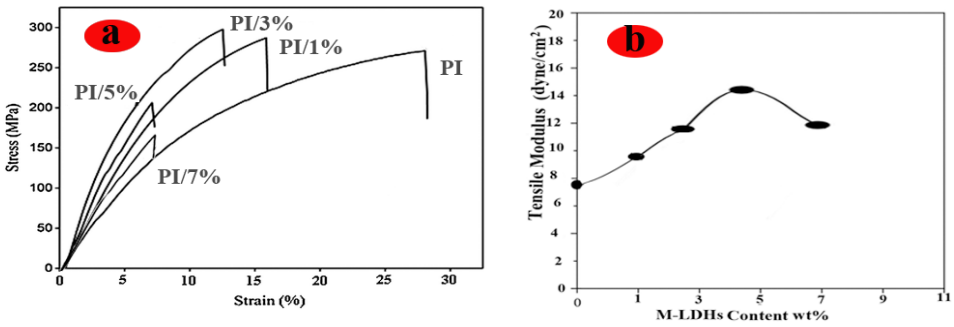

Fig. 6. (a) Stress/strain curves of M-LDHs/PI nanocomposite film with various M-LDHs nanoparticles contents. (b) Effect of the M-LDHs content on the tensile modulus of the film nanocomposites.

on the thermomechanical properties of PI films. The storage modulus (E′) and loss modulus (E″) with various M-LDHs contents are shown in Fig. 5 (a) and the values of tan δ are shown in Fig. 5 (b). A small decrease in the storage modulus was observed around T_g in Fig. 5 (a), which is typical for rigid rod PI. Fig. 5 (c) shows the effect of the M-LDHs particles content on the T_g from the maxima of E″ curves. It was confirmed that the T_g values increased with an increase in the M-LDHs particles content: T_gs were 329, 354, 361, and 351°C at the M-LDHs particles content of 1, 3, 5 and 7 wt. %, respectively. The tan δ values in Fig. 5 (b) also show that the T_gs increased above 400 °C with addition of 1% of M-LDHs. Since the glass transition process is related to the molecular motion, the T_g is considered to be affected by molecular packing, chain rigidity and linearity. The increase in the T_g values of the nanocomposites in comparison with the original PI can be attributed to maximizing the adhesion between the PI and M-LDHs surfaces because of the nanometer size which restricts segmental motion near the organic inorganic interface. This is a typical effect for the inclusion of M-LDHs in a polymer system.

The tensile properties of the M-LDHs/PI nanocomposites hybrid films were examined. As summarized in Table 1, there was a clear tendency that the tensile modulus increases and elongation decreases with an increase in the content of M-LDHs nanoparticles. For pure PI, which was thermally treated at 350°C/15 min, the tensile modulus was 7.85 GPa. With the incorporation of 1% M-LDHs nanoparticles, the tensile modulus increased to ca. 9.86 GPa, which is ca. 44% higher than that of the original PI. The increase in the modulus was accompanied with 67% decrease in the elongation at break. Addition of 3% of M-LDHs nanoparticles further increased the modulus to 11.68 GPa, which is ca. 110% higher than the pristine PI. It was reported from the viscoelastic analyses that the storage modulus of PI increased up to 20% by the inclusion of clay compared to the pristine PI [37, 38]. Thus the tensile measurements revealed that the effect of the M-LDHs nanoparticles is more pronounced on the tensile modulus. The pronounced increase in the tensile modulus reflects the reinforcement effect attained by the dispersion of the M-LDHs nanoparticles into PI film. Elongation at break, on the other hand, decreased monotonously to 15%. A further increase in the M-LDHs nanoparticles content (5%) is associated with a decrease in the modulus and a sharp elongation at break which is ca. 2%.

Fig. 6 (a) shows typical stress/strain curves for M-LDHs/PI nanocomposites. The tensile modulus of pristine PI film, which was thermally treated at

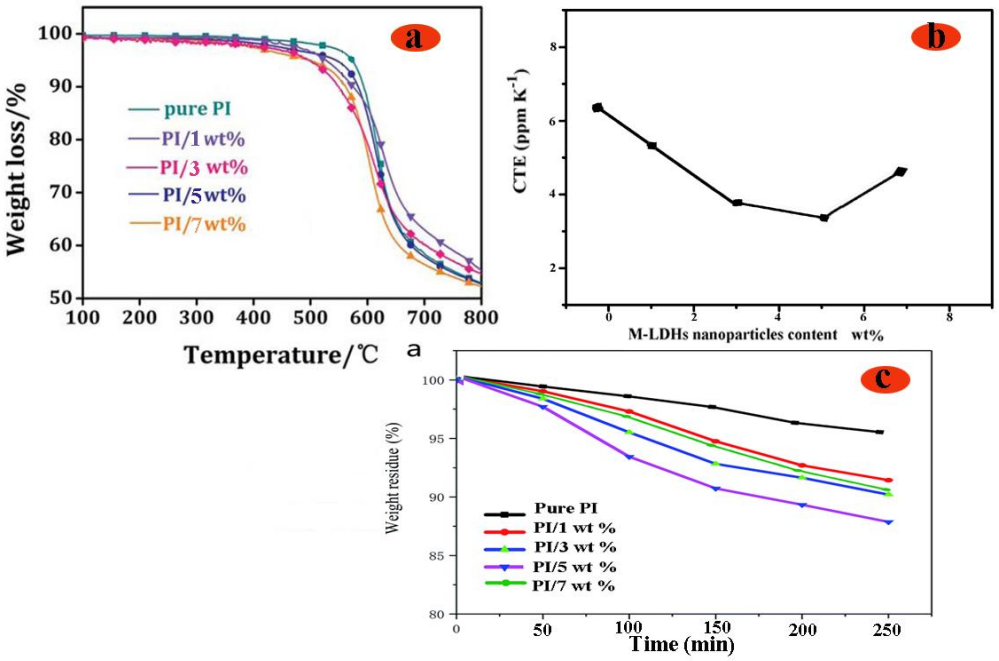

Fig. 7. (a) TGA of M-LDHs/PI nanocomposite, (b) effect of M-LDHs content on the CTE of M-LDHs/PI nanocomposite films, (c) isothermal TGA of M-LDHs/PI nanocomposite at 500°C for 250 min.

350 ° C/1 h, was 12.15 GPa. With incorporation of 1% M-LDHs nanoparticles, the tensile modulus increased to 16.55 GPa. Addition of 3% of M-LDHs nanoparticles further increased the modulus to 19.85 GPa, which is 39% higher than that for the pristine PI. The pronounced increase in the tensile modulus reflects the reinforcement effect attained by the dispersion of the M-LDHs nanoparticles into PI film. Elongation at break, on the other hand, decreased monotonously. Tensile strength increased with 1% of clay loading, but started to decrease at relatively low loading of M-LDHs because of the lower elongation at break. With 5% M-LDHs nanoparticles content the tensile modulus started to decrease to 10.25 GPa. Also, the drop in the tensile properties was remarkable in the case of higher M-LDHs nanoparticles loading such as M-LDHs/PI 7% (Fig. 6(a)). This collapse of the mechanical properties can be attributed to the aggregation of the M-LDHs nanoparticles. The effect of M-LDHs nanoparticles loading on the tensile modulus of PI is shown in Fig. 6 (b). The increase of tensile modulus is mainly based on the reinforcement effect of the dispersed M-LDHs nanoparticles. The additional effect due to the chain orientation in PI should be minimum.

Thermal behavior of pure PI and M-LDHs/PI nanocomposites

TGA was recorded for M-LDHs/PI nanocomposites to monitor the effect of the M-LDHs particles on the thermal properties. Fig. 7 (a) shows some results of TGA in case of M-LDHs/PI nanocomposite. It was shown that the thermal stability increased with addition of M-LDHs nanoparticles. The temperatures at 5 and 10% weight loss indicate that the thermal stability of the PI films was enhanced by the incorporation of only small amount of LDHs nanoparticles. For example, with only 1% content of LDHs particles in the PI, the 5% decomposition temperature became higher for ca. 208 °C than the corresponding pure PI. Above 5% loading, the effect of LDHs particles was almost constant; probably due to the aggregation of the additional LDHs. The presence of M-LDHs particles dispersed homogeneously into the PI film hinders the permeability of volatile degradation products out of the material. Fig. 7 (c) shows the isothermal TGA for M-LDHs/PI nanocomposites at 500 °C for 250 min. As clearly seen, the nanocomposites show a delayed decomposition compared with the pure PI due to the homogeneous distribution of the M-LDHs

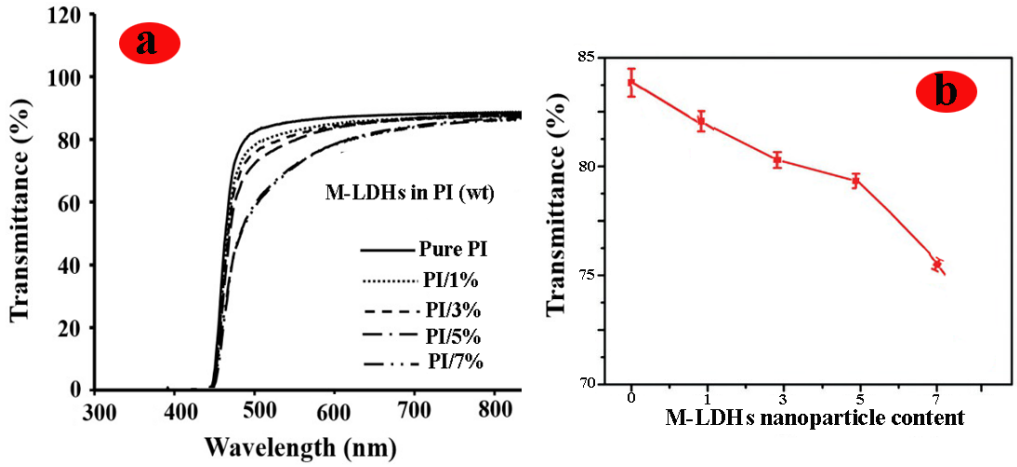

Fig. 8. (a) UV–Vis spectra of pure PI and M-LDHs/PI nanocomposite films with various contents of the M-LDHs nanoparticles. (b) The transmittance of all films at 780 nm.

nanoparticles which increases the total path of the volatile gases out of the film compared to the pure PI. For PI, the incorporation of the M-LDHs particles also enhanced the thermal stability.

Fig. 7b shows the effect of the inclusion of the M-LDHs particles on the coefficient of thermal expansion (CTE) of PI films. It was found that the CTE decreased from 6.47 ppm (0% M-LDHs particles) to 5.36 ppm (1% M-LDHs particles) and 3.88 ppm (3% M-LDHs particles) and 3.26 ppm (5% M-LDHs particles) with the increase of M-LDHs particles content up to 1% loading. The CTE, however, increased with increase of the M-LDHs particles content above 5%. This tendency is in accordance with the change of the tensile modulus.

Optical properties of M-LDHs/PI nanocomposites

Optical appearance is an acceptable and convenient method in judging the dispersion of inorganic phase in polymer matrix. If the polymer/inorganic nanocomposites are transparent, the inorganic phase can be well dispersed in the polymer matrix. The variation of transparency values with wavelength for PI and M-LDHs/PI nanocomposite films is shown in Fig. 8a. It was found that the composite films lose their transparency when the clay content further increases. Two quantities, the transmission onset and the 86% transmission wavelength, are usually used to evaluate the transparency of these films [39]. They range from 450 to 465 nm for the onset wavelength, and from 550 to 800 nm for the 85% transmission wavelength. The transmittance of all films at 780 nm is given in Fig. 8b. When the M-LDHs nanoparticle content increases from 1 to 5 wt% in PI matrix, the transmittance of nanocomposite films slightly decreases. But when M-LDHs nanoparticles content is more than 5 wt%, the transparency of films rapidly decreases. This is an evidence for a poor dispersion of M-LDHs nanoparticles in PI matrix, and this phenomenon is consistent with the results of FE-SEM and TEM (Figs. 3 and 4).

Gas permeation properties of pure PI and M-LDHs/PI nanocomposite films

Gas permeability investigation of nanocomposite films based on both types of M-LDHs nanoparticles was performed using pure gases He, N_2, CH_4 and CO_2 and the results are summarized in Table 2. For all types of M-LDHs/PI nanocomposite films, an overall decrease in permeability for all gases was observed in comparison to that of pure PI. This could be attributed to an increase in tortuous path length as well as to closer PI chain packing in M-LDHs/PI nanocomposite films in comparison to the pure PI (as revealed by lowering in d_{sp}). The d_{sp} of pure PI and M-LDHs/PI (1, 3, 5 and 7%) is 6.42, 5.88, 5.47, 5.24 and 4.98 , respectively. Various polymer/clay nanocomposites exhibited a large decrease in permeability for different gases [29, 30, 40–42], as also observed in the present case. This could be attributed to the lower available free volume in earlier cases at a particular loading level. This was indicated by a decrease in d_{sp} of the polymer fraction in the nanocomposites, as a result of suitable interaction of M-LDHs with PI

Table 2. Permeability coefficient (P)[a] and selectivities (α)[b] for nanocomposites with different percent loadings of M-LDHs nanoparticles

	Pure PI	M-LDHs/PI 1%	M-LDHs/PI 3%	M-LDHs/PI 5%	M-LDHs/PI 7%
He	50.23	42.32	39.86	35.28	33.57
N_2	2.21	1.89	1.45	1.08	0.89
CH_4	1.88	1.58	1.25	0.98	0.45
CO_2	45.69	24.96	18.65	10.89	6.32
α(He/N_2)	22.72	22.39	27.48	32.66	37.71
α(He/CH_4)	2 6.71	26.78	31.88	36	74.6
α(He/CO_2)	1 .09	1.69	2.13	3.23	5.31
α(CO_2/N_2)	2 0.67	13.20	12.86	10.08	6.44
α(CO_2/CH_4)	2 4.30	15.79	14.92	14.11	11.04

[a]Permeability expressed in Barrer (1 Barrer = 1×10^{-10} cm^3 (STP) cm cm^{-2} s^{-1} cm Hg^{-1}). [b]Ratio of pure gas permeability.

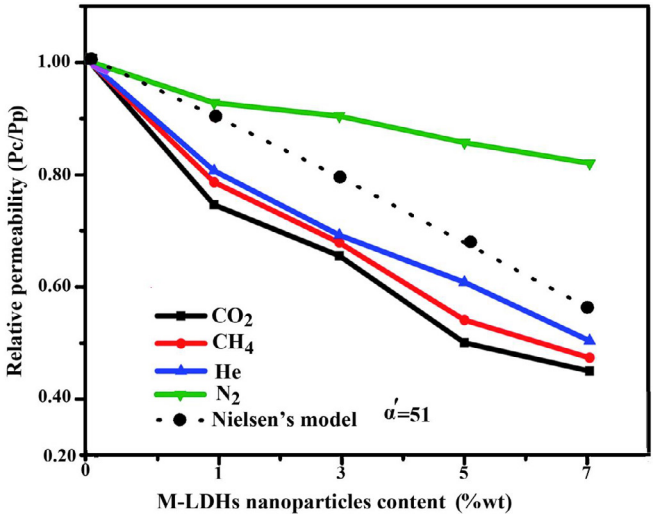

Fig. 9. Variation of relative permeability (*Pc*/*P*p) with volume fraction (φ_f) of M-LDHs nanoparticles based PI nanocomposites.

and observed higher density and solution viscosity for M-LDHs nanocomposites. Variation in relative permeability (M-LDHs/PI) with the volume fraction of M-LDHs loading is presented in Figs. 9 for M-LDHs nanocomposites. This ratio decreased with increased M-LDHs loading from 3 to 7%. This trend could be anticipated based on increased tortuous path for diffusing molecules. The reduction in relative permeability for different gases was observed to be different for a particular membrane. In butyl rubber/vermiculite membranes, the relative permeability for various gases differed by as much as a factor of two for a given membrane [43]. A nominal aspect ratio (α′) is usually calculated by fitting the relative permeability data as the function of clay content [29, 40, and 42]. From the trend obtained in the reduction in He permeability (Figs. 9), α' was estimated by following Nielsen's model (Eq. (1)) developed for depicting barrier properties of nanocomposites containing platelet particles [31].

$$Pc = Pp(\frac{1-\phi f}{1+\alpha'\phi/2})$$

where *Pc* and *Pp* are the permeability of the nanocomposites medium and the pure polymer, respectively, and ϕ_f is the volume fraction of the filler. Helium gas was chosen to estimate α′ using Eq. (2) in view of non-interacting nature of this gas. Transport of He would be diffusion controlled [41] and more accurate prediction of α′ could thus be possible. For nanocomposites based on M-LDHs nanoparticles, α′ was estimated to be 51. This indicated higher level of M-LDHs nanoparticles dispersion in PI based nanocomposites. This was in an agreement with XRD and TEM analyses of PI based nanocomposites, indicating suitable

dispersion of M-LDHs nanoparticles in the polyimide matrix. As seen in Fig. 9, reduction in He permeability variation is considerably more than that for other gases such as CH_4 and CO_2. It could be anticipated that in addition to diffusion, permeability variations of these gases could also be contributed by sorption component. Owing to this, Nielsen's model cannot be directly applied for these gases in the present case. Wang et al. [43] has reported reduction in diffusion (59.5%) as well as in calculated solubility (22.9%) for N_2 in rectorite/SBR composites. Ryu and Chang [41] also observed that variation in the relative permeability of O_2, N_2 and CO_2 was different at certain MMT content in LLDPE. According to the simple composite theory [40], tortuosity factor depends on the content of particles, their shape, location and orientation in space, and it is not affected by the absolute particle size or the type of penetrant. Variations observed in the reduction of permeability for different gases as reported in the literature [29, 30, 40,41] and also in the present case does not seem to support this composite theory completely. The reduction in permeability may also depend upon the size and condensability of penetrant gas molecules. The gas permeability in polymer matrix is governed by solubility (affected by condensability and membrane–penetrant interactions) as well as diffusivity (affected by size and shape of the penetrant). Based on the literature[29, 44] both of these basic properties are affected by polymer–clay nanocomposite formation. It was observed that for He, diffusion rather than solubility was responsible for the reduction in the permeability, while for N_2 and O_2, both diffusivity and solubility were reduced by the presence of clay-fillers in PP–clay nanocomposites [45]. It was also stated that for more condensable gases, interactions along the clay–PP matrix interface may affect the gas sorption process in the polymer membrane. In the present case, gas sorption and diffusion analysis though could not be performed; an increase in packing density of polymer chains (as revealed by decrease in d_{sp}) probably affected both solubility and diffusivity. Variations in packing density in the same family of polymers by structural variations are known to vary both these crucial parameters responsible for permeation. Thus, the simple composite theory may not be sufficient to explain variations in gas permeability caused by nanocomposites formation, and gas solubility needs to be considered in addition to the diffusion. Increased CO_2 sorption in butyl rubber–vermiculite nanocomposite [40], decreased sorption of O_2 and N_2 in PP–clay nanocomposite [30], increase in free volume for molecular transport in case of poly(1-trimethylsilyl-1-propyne) [42] and poly(4-methyl-2-pentyne) [43] could be as some of the optimistic examples indicating that with a proper selection of polymer and filler type, it may be possible to widen the difference between relative permeability variations of different gases. In other words, this can be utilized as a tool to drive selectivity of particular gas pair in a desired direction.

Effect on selectivity of nanocomposite films

Variation in the selectivity for different gas pairs in comparison to the selectivity of pure PI (Table 2) showed a complex trend at different M-LDHs nanoparticles loadings resulting in nanocomposites. $\alpha(He/CO_2)$ was increased up to five times, while $\alpha(CO_2/N_2)$ and $\alpha(CO_2/CH_4)$ were decreased at all the loading percentages. A larger decrease in permeability of CH_4 than for He, particularly at 7% loading, led to a considerable increase in $\alpha(He/CH_4)$. A 2.7 times increase in $\alpha(He/O_2)$ in PP–clay nanocomposite was reported [30]. The CO_2 based selectivities, $\alpha(CO_2/N_2)$ and $\alpha(CO_2/CH_4)$, in the present case were reduced dramatically as a result of larger drop in CO_2 permeability (48–88%) than for either N_2 or CH_4 (up to 69%) for different nanocomposite membranes. The greater reduction in permeability of CO_2 than that in N_2 and CH_4 is an anomalous behavior. Both the contributing factors to permeability, i.e. diffusivity and/or solubility cannot be anticipated to be reduced based solely on established assumptions. Reduction in the diffusivity may not be just based on kinetic diameter of CO_2, which is smaller than that of N_2 and CH_4. Similarly, sorption of CO_2 in polymer matrix is usually much higher than that of N_2 and CH_4 in most of the polymeric materials. At least for the type of polymer used here (polyimide) this is well established. There could be some other factors responsible for this observed anomaly. It was observed that for a particular case of benzoylation of PPO, reduction in gas permeability for different gases follows the order: $He < CH_4 < N_2 < CO_2$, which was in the order of their increasing molar mass and not the kinetic diameter [43-44, 45-47]. Thus, in addition to kinetic diameter, other properties of CO_2 (molar mass or cylindrical nature) may also be responsible for execution of 'diffusion jump' from one activated site to another. This issue needs

more investigations and supporting evidences. An increase in He/CH_4 selectivity could be seen only at 7% loading, indicating that there could be a bare minimum requirement for M-LDHs loading to affect the selectivity favorably in these PI based nanocomposites. This could be possible especially in view of the presence of long amino benzoate chain of organic modifier of the LDHs. Though such modifier is required to induce compatibility of the LDHs with polymer chains, it is usually composed of long chains, which can also induce plasticization as observed by decrease in glass transition temperature in the present case. This decrease in T_g could be anticipated to adversely affect the selectivity performance owing to poorer penetrant-discriminating ability due to plasticization. A smaller variation in α(He/CH_4) selectivity at 3–5% loading suggested that probably this plasticization effect is more predominant than the tortuous path offered at this loading level in governing selectivity, while at 7% loading, much higher tortuous path may be predominantly responsible to reduce permeability of larger gases, leading to higher selectivity of He/CO_2 and He/CH_4 pairs. In order to tune selectivity favorably, selection of amino benzoate group modifier (intercalant/surfactant) that would show minimal plasticization effect and at the same time facilitate maximum possible interactions (may be exfoliation) may be required. Variation in other physical properties by nanocomposites formation that governs gas sorption and diffusion can also be crucial.

CONCLUSION

Novel polyimide (PI) nanocomposite films were synthesized from diamine monomer and pyromellitic dianhydride (PMDA) with various modified layered double hydroxides (LDHs) particles via solution intercalation polymerization to poly(amic acid)s, followed by thermal imidization. Modified LDHs particles, including LDH-amino benzoate (M-LDHs) were prepared with coprecipitation method. The intercalation of PI chains among the LDHs particles was examined using wide-angle X-ray diffraction (XRD) and electron microscopy (TEM) techniques. TEM photographs showed that most LDH layers were dispersed homogeneously into the matrix polymer on the nanoscale, although some LDHs particles were agglomerated. Moreover, the addition of only a small amount of LDHs particles was enough to improve the thermal stabilities and mechanical properties of PI hybrid films. The thermo-optical properties were measured by differential scanning calorimetry (DSC), thermogravimetric analysis (TGA), and ultraviolet-visible (UV–Vis) spectrometry. As anticipated, though the gas permeability of pure gases such as He, N_2, CH_4 and CO_2 exhibited a decrease, it was not monotonous. A marked decrease in permeability of gases like CO2 and CH4, in comparison to relatively lower decrease in permeability of He was observed, especially at higher LDH loading. An increase in selectivity: α(He/CO2) and α(He/CH4), especially at higher LDH loading indicated the capability of nanocomposites to tune the selectivity favorably.

We used TEM to evaluate the degree of intercalation and the amount of aggregation of the M-LDHs nanoparticles. The M-LDHs nanoparticles, for the most part, were well dispersed in the polymer matrix.

From thermal properties it was shown that the thermal stability increased with addition M-LDHs nanoparticles. The temperatures at 5 and 10% weight loss are which indicates that the thermal stability of the PI films was enhanced by the incorporation of only small amount of LDHs nanoparticles. T_gs of the nanocomposites were higher than that of the pure PI.

The tensile modulus was enhanced by the inclusion of the M-LDHs nanoparticles into the PI matrix, accompanied with a decrease in the elongation at break. The increase in the tensile modulus is almost solely to the reinforcement effect of the dispersed M-LDHs nanoparticles. The effect of chain orientation was considered to be minimum, if any.

Overall decrease in permeability for all the gases was observed with incremental loading of M-LDH snanoparticles. Predicted aspect ratio by Nielsen's model for both the nanocomposites was in agreement with the observed variation in physical properties of polyimide based nanocomposites. Marked decrease in permeability of gases like CO_2 and CH_4, in comparison to relatively lower decrease in permeability of He was observed, especially at higher M-LDHs nanoparticles loading. An increase in selectivity: α(He/CO_2) and α(He/CH_4), especially at higher M-LDHs nanoparticles loading indicated the capability of nanocomposites to tune the selectivity favorably. A bare minimum requirement of M-LDHs nanoparticles loading to successfully overcome the effect of plasticization towards lowering in selectivity was noted. This

indicated that if amino benzoate group modifier could be chosen such that it would minimize plasticization and facilitates clay exfoliation while inducing compatibility of M-LDHs nanoparticles with polymer chains, the permeation properties, especially selectivity behavior could be better tuned.

ACKNOWLEDGEMENTS

The authors thank darab branch, Islamic Azad University for the financial support.

CONFLICT OF INTEREST

The authors declare that they have no conflict of interest.

REFERENCES

1. Liu Z, Xu J, Chen D, Shen G. Flexible electronics based on inorganic nanowires. Chemical Society Reviews. 2015;44(1):161-92.
2. Liu J-M, Lee TM, Wen C-H, Leu C-M. High-performance organic-inorganic hybrid plastic substrate for flexible displays and electronics. Journal of the Society for Information Display. 2011;19(1):63.
3. Shin HI, Chang J-H. Transparent Polyimide/Organoclay Nanocomposite Films Containing Different Diamine Monomers. Polymers. 2020;12(1):135.
4. Mativenga M, Choi MH, Choi JW, Jang J. Transparent Flexible Circuits Based on Amorphous-Indium–Gallium–Zinc–Oxide Thin-Film Transistors. IEEE Electron Device Letters. 2011;32(2):170-2.
5. Yu X, Zhao X, Liu C, Bai Z, Wang D, Dang G, et al. Synthesis and properties of thermoplastic polyimides with ether and ketone moieties. Journal of Polymer Science Part A: Polymer Chemistry. 2010;48(13):2878-84.
6. Garg P, Singh RP, Pandey LK, Choudhary V. Pervaporative studies using polyimide-filled PDMS membrane. Journal of Applied Polymer Science. 2010;115(4):1967-74.
7. Surya R, Mullassery MD, Fernandez NB, Thomas D. Synthesis and characterization of a clay-alginate nanocomposite for the controlled release of 5-Flurouracil. Journal of Science: Advanced Materials and Devices. 2019;4(3):432-41.
8. Liou H-C, Willecke R, Ho PS. Study of out-of-plane elastic properties of PMDA-ODA and BPDA-PDA polyimide thin films. Thin Solid Films. 1998;323(1-2):203-8.
9. Suhail MH, Abdullah OG, Kadhim GA. Hydrogen sulfide sensors based on PANI/f-SWCNT polymer nanocomposite thin films prepared by electrochemical polymerization. Journal of Science: Advanced Materials and Devices. 2019;4(1):143-9.
10. Chen C-J, Yen H-J, Hu Y-C, Liou G-S. Novel programmable functional polyimides: preparation, mechanism of CT induced memory, and ambipolar electrochromic behavior. Journal of Materials Chemistry C. 2013;1(45):7623.
11. Zheng Y, Chen Y. Preparation of polypropylene/Mg–Al layered double hydroxides nanocomposites through wet pan-milling: formation of a second-staging structure in LDHs intercalates. RSC Advances. 2017;7(3):1520-30.
12. Zhao Y, Li N, Yuan F, Zhang H, Xia S. Preparation and characterization of hydrophilic and antifouling poly(ether sulfone) ultrafiltration membranes modified with Zn-Al layered double hydroxides. Journal of Applied Polymer Science. 2016;133(39).
13. Suresh K, Kumar M, Pugazhenthi G, Uppaluri R. Enhanced mechanical and thermal properties of polystyrene nanocomposites prepared using organo-functionalized Ni Al layered double hydroxide via melt intercalation technique. Journal of Science: Advanced Materials and Devices. 2017;2(2):245-54.
14. Sinha Ray S, Okamoto M. Polymer/layered silicate nanocomposites: a review from preparation to processing. Progress in Polymer Science. 2003;28(11):1539-641.
15. Newman SP, Jones W. Synthesis, characterization and applications of layered double hydroxides containing organic guests. New Journal of Chemistry. 1998;22(2):105-15.
16. Chubar N, Szlachta M. Static and dynamic adsorptive removal of selenite and selenate by alkoxide-free sol–gel-generated Mg–Al–CO 3 layered double hydroxide: Effect of competing ions. Chemical Engineering Journal. 2015;279:885-96.
17. Richardson-Chong SSD, Patel R, Williams GR. Intercalation and Controlled Release of Bioactive Ions Using a Hydroxy Double Salt. Industrial & Engineering Chemistry Research. 2012;51(7):2913-21.
[18] Wang Q. Polypropylene/Mg_3Al–tartrazine LDH nanocomposites with enhanced thermal stability, UV absorption, and rheological properties. RSC advances. 2013;v. 3(no. 48):pp. 26017-24-2013 v.3 no.48.
19. Zhang S, Liu X, Gu X, Jiang P, Sun J. Flammability and thermal behavior of polypropylene composites containing dihydrogen phosphate anion-intercalated layered double hydroxides. Polymer Composites. 2014;36(12):2230-7.
20. Min U, Yoon CS, Chang J-H. Characterizations of transparent polyimide nanocomposite films with various equibiaxial stretching ratios: Optical transparency, morphology, and oxygen permeability. Journal of Applied Polymer Science. 2012;126(S2):E2-E11.
21. Ahmadizadegan H, Khajavian R. Novel functional aromatic polyimides and polyimide/titania nanocomposite thin films for gas separation: preparation and structural characterization. Journal of the Iranian Chemical Society. 2016;14(4):777-89.
22. Pinnavaia TJ. Intercalated Clay Catalysts. Science. 1983;220(4595):365-71.
23. Chuang S-W, Hsu SL-C, Hsu C-L. Synthesis and properties of fluorine-containing polybenzimidazole/montmorillonite nanocomposite membranes for direct methanol fuel cell applications. Journal of Power Sources. 2007;168(1):172-7.
24. Liu P. Polymer modified clay minerals: A review. Applied Clay Science. 2007;38(1-2):64-76.
25. Lan T, Kaviratna PD, Pinnavaia TJ. On the Nature of Polyimide-Clay Hybrid Composites. Chemistry of Materials. 1994;6(5):573-5.
26. Bharadwaj RK. Modeling the Barrier Properties of Polymer-Layered Silicate Nanocomposites. Macromolecules. 2001;34(26):9189-92.
27. Nielsen LE. Models for the Permeability of Filled Polymer Systems. Journal of Macromolecular Science: Part A - Chemistry. 1967;1(5):929-42.
[28] Mittal V. Barrier properties of polymer clay nanocomposites:

Nova Science Publishers; 2010.
29. Bhole YS, Wanjale SD, Kharul UK, Jog JP. Assessing feasibility of polyarylate–clay nanocomposites towards improvement of gas selectivity. Journal of Membrane Science. 2007;306(1-2):277-86.
30. Villaluenga JPG, Khayet M, López-Manchado MA, Valentin JL, Seoane B, Mengual JI. Gas transport properties of polypropylene/clay composite membranes. European Polymer Journal. 2007;43(4):1132-43.
31. Okada A, Usuki A. The chemistry of polymer-clay hybrids. Materials Science and Engineering: C. 1995;3(2):109-15.
32. Ahmadizadegan H, Esmaielzadeh S, Ranjbar M, Marzban Z, Ghavas F. Synthesis and characterization of polyester bionanocomposite membrane with ultrasonic irradiation process for gas permeation and antibacterial activity. Ultrasonics Sonochemistry. 2018;41:538-50.
33. Kim Y, Chang J-H, Kim J-C. Optically transparent and colorless polyimide hybrid films with various clay contents. Macromolecular Research. 2012;20(12):1257-63.
34. Atabaki F, Ahmadizadegan H. Fabrication of a New Polyimide/Titania (TiO2) Nanocomposite Thin Film by the Sol-Gel Route. Polymer-Plastics Technology and Engineering. 2015;54(5):523-31.
35. Phan TTM, Chu NC, Luu VB, Nguyen Xuan H, Pham DT, Martin I, et al. Enhancement of polarization property of silane-modified BaTiO 3 nanoparticles and its effect in increasing dielectric property of epoxy/BaTiO 3 nanocomposites. Journal of Science: Advanced Materials and Devices. 2016;1(1):90-7.
36. Choi IH, Chang J-H. Colorless polyimide nanocomposite films containing hexafluoroisopropylidene group. Polymers for Advanced Technologies. 2011;22(5):682-9.
37. Yano K, Usuki A, Okada A, Kurauchi T, Kamigaito O. Synthesis and properties of polyimide–clay hybrid. Journal of Polymer Science Part A: Polymer Chemistry. 1993;31(10):2493-8.
38. Agag T, Koga T, Takeichi T. Studies on thermal and mechanical properties of polyimide–clay nanocomposites. Polymer. 2001;42(8):3399-408.
39. Shin J, Kim J-C, Chang J-H. Flexible clay hybrid films with various poly(vinyl alcohol) contents: Thermal properties, morphology, optical transparency, and gas permeability. Macromolecular Research. 2013;21(12):1349-54.
40. Takahashi S, Goldberg HA, Feeney CA, Karim DP, Farrell M, O'Leary K, et al. Gas barrier properties of butyl rubber/vermiculite nanocomposite coatings. Polymer. 2006;47(9):3083-93.
41. Ryu SH, Chang Y-W. Factors affecting the dispersion of montmorillonite in LLDPE nanocomposite. Polymer Bulletin. 2005;55(5):385-92.
42. Merkel TC, He Z, Pinnau I, Freeman BD, Meakin P, Hill AJ. Effect of Nanoparticles on Gas Sorption and Transport in Poly(1-trimethylsilyl-1-propyne). Macromolecules. 2003;36(18):6844-55.
43. Merkel TC, Freeman BD, Spontak RJ, He Z, Pinnau I, Meakin P, et al. Sorption, Transport, and Structural Evidence for Enhanced Free Volume in Poly(4-methyl-2-pentyne)/Fumed Silica Nanocomposite Membranes. Chemistry of Materials. 2003;15(1):109-23.
44. Wang ZF, Wang B, Qi N, Zhang HF, Zhang LQ. Influence of fillers on free volume and gas barrier properties in styrene-butadiene rubber studied by positrons. Polymer. 2005;46(3):719-24.
[45] Ahmadizadegan H. Effect of adding Nanoclay (Cloisite-30B) on the Proton Conductivity of Sulfonated Polybenzimidazole. Nanochemistry Research. 2017;2(1):96-108.
46. Bhole YS, Kharul UK, Somani SP, Kumbharkar SC. Benzoylation of polyphenylene oxide: Characterization and gas permeability investigations. European Polymer Journal. 2005;41(10):2461-71.
47. Ahmadizadegan H. Synthesis and gas transport properties of novel functional polyimide/ZnO nanocomposite thin film membranes. RSC Advances. 2016;6(108):106778-89.